



Fabrication and characterization of aluminum foam reinforced with nanostructured γ -Al₂O₃ via friction stir process for enhanced mechanical performance

Ioannis G. Papantoniou^{1,2} · Dimitrios E. Manolakos¹

Received: 2 November 2023 / Accepted: 14 January 2024 / Published online: 23 January 2024
© The Author(s) 2024

Abstract

This study focuses on the fabrication and characterization of aluminum foam reinforced with nanostructured γ -Al₂O₃, utilizing AA5083 plates. The fabrication process involved the integration of TiH₂ foaming agent particles and reinforcing nanoparticles via the friction stir process (FSP), resulting in the creation of precursor specimens. Subsequently, a separate foaming stage was conducted within a laboratory furnace. The integration of these particles was achieved through the machining of parallel grooves in a single aluminum plate. The initial phase of the experimental study focused on investigating the effect of varying amounts of the foaming agent. Large-scale foams were then produced, achieving a medium porosity of 70%. Electro-discharge machining was employed to prepare specimens for compression testing to analyze their stress–strain response. The results revealed a plateau stress of 27 MPa, a relative Young’s modulus of 4.44×10^{-3} , and an energy absorption close to 17 MJ/m³ at 50% strain. Significantly enhanced plateau stress was observed in the manufactured reinforced aluminum foam compared to similar foams produced through conventional methods.

Keywords Porous metals · Composite metal foams · Friction stir processing · Friction stir welding · γ -Al₂O₃ nanopowder · Mechanical properties

1 Introduction

Cellular metallic materials offer a blend of versatile properties within a lightweight structure, making them well-suited for diverse applications across industries such as automotive, aviation, vibration control, and structural components [1].

The production of cellular metallic materials encompasses a diverse range of manufacturing approaches. Some of these methods share similarities with techniques used in creating foams from aqueous or polymer liquids. Conversely, others are uniquely crafted to harness the inherent properties of metals, such as their sintering capabilities or their suitability for electrical deposition [2]. Specifically, when it

comes to crafting aluminum foams, a variety of techniques are available. Among these methods, the precursor-based indirect approach emerges as a noteworthy method for generating closed-cell porous aluminum. In this process, a blowing agent, typically TiH₂, is integrated into the aluminum matrix, resulting in the formation of a precursor specimen. Subsequently, the precursor undergoes a heat treatment procedure, causing the blowing agent to decompose and release gases that lead to the expansion of the aluminum alloy [3, 4].

It is worth noting that the precursor-based indirect approach primarily employs base materials in the form of powders, necessitating the application of powder metallurgy techniques. However, the use of powders introduces various challenges in the production of aluminum foams. In response to these challenges, the friction stir process (FSP) method emerged as a novel solution. FSP stands out as an innovative metalworking technique rooted in the fundamental principles of friction stir welding (FSW) [5–7]. This method facilitates localized manipulation and precise control of microstructures within the near-surface layers of metallic components, resulting in the development of tailored microstructures and nanocomposite materials [8–10]. By harnessing high

✉ Ioannis G. Papantoniou
ipapanto@central.ntua.gr

¹ School of Mechanical Engineering, Laboratory of Manufacturing Technology, National Technical University of Athens, Athens, Greece

² Department of Naval Architecture, School of Engineering, University of West Attica, 12243 Egaleo, Greece

temperatures and strain rates, FSP induces microstructural modifications, establishing itself as a versatile and environmentally friendly solid-state fabrication approach [11, 12]. In the FSP process, a cylindrical tool equipped with a shoulder and a pin traverses the workpiece's surface [13, 14]. The tool's shoulder engages with the surface, generating frictional heat that softens the material underneath. The rapid rotation of the pin subjects the softened material to high strain rates, inducing deformation and prompting a transformative shift in its microstructure. The versatility of FSP extends to its applicability in diverse industrial sectors, including aerospace and automotive industries [15, 16].

Hangai et al. [17, 18] introduced the development of aluminum foams using the FSP process. Their approach involved the application of FSP to AA4045 and AA1050 alloys, resulting in the creation of aluminum foams. The process involved the stacking of two aluminum plates and placing the blowing agent and stabilizing/reinforcing agents in the middle. Through the FSP process, they effectively integrated the blowing and stabilizing/reinforcing agents into the aluminum plates, forming precursor materials. Subsequently, these precursor materials underwent controlled heat treatment to initiate the foaming process. This approach eliminates the reliance on powder metallurgy techniques, addressing challenges associated with powder usage. The outcomes of the study revealed a direct relationship between increased foaming temperatures and a higher number of FSP passes, leading to a corresponding increase in porosity. A similar methodology employing stacked plates was also adopted by Utsunomiya et al. [19] for the production of metal foam from AA6061. Additionally, Saito et al. [20] employed this approach to fabricate functionally graded aluminum foam, combining A1050 and A6061 aluminum alloys.

An alternative approach to manufacturing aluminum foams through the FSP process was implemented by Papanthiou et al. [21, 22]. This method introduces a distinctive innovation wherein a single aluminum plate serves as the foundational material, with foaming and reinforcing particles strategically placed within a machined groove. This approach enabled the creation of localized, reinforced foamed regions within the metal components, thereby customizing the mechanical and physical properties of these parts.

However, while the single-plate approach presents notable advantages in tailoring these properties, it encounters limitations when determining the mechanical response due to the relatively confined volume of the foamed region. Hence, in our present investigation, we have undertaken the development of large-scale foams by incorporating multiple grooves within a single aluminum plate. This evolution in methodology serves a dual purpose: first, to analyze the mechanical compressive response of specimens on a larger scale, and second, to explore the capabilities of the

single-plate approach in producing extensive reinforced aluminum foams.

2 Materials and methods

2.1 Materials

The base metallic alloy selected for this study was the AA5083-H111, provided in the form of 6 and 8-mm-thick plates. AA5083 was chosen for its work-hardened characteristics, with the anticipation of minimal softening during the FSP. However, it is acknowledged that there might be a slight softening effect due to the potential compromise of work-hardening effects. Secondly, the high magnesium content (>4%) in the alloy is anticipated to enhance the bonding and wetting of the reinforcing particles [23].

In this research, laboratory-produced nanosized γ -Al₂O₃ powder (with an average particle size of 5 nm) was used as reinforcing and stabilizing agents. Additionally, the blowing agent employed for the foaming process was commercially available titanium hydride powder, characterized by a particle diameter of less than 45 μ m.

2.2 FSP-based manufacturing procedure

The research comprises two distinct phases. The initial preliminary phase of the experimental study focused on exploring the effects of varying the foaming agent's quantity. In this phase, single grooves (1 mm wide, 3 mm deep) were precisely machined parallel to the rolling direction of the 6-mm-thickness plates and aligned with the centerline of the rotating pin. Different amounts of TiH₂ were employed (0.3% w/w, 0.5% w/w, 0.7% w/w, 0.9% w/w, respectively) to examine their impact on the final porosity. FSP was utilized for the integration of the particles into the aluminum matrix, and a separate foaming stage was conducted within a laboratory furnace. The manufacturing process is illustrated in Fig. 1 and is further analyzed in the corresponding research [22].

Building upon the results of the preliminary phase, the research's second and main phase involved the development of large-scale foams. As depicted in Fig. 2, multiple grooves were machined at the 8-mm-thickness plates at a consistent distance of 7 mm (center to center). The precursor specimen/plate was created by blending blowing agent powder (0.9% w/w TiH₂) and stabilization agent nanopowder (2% w/w γ -Al₂O₃). This mixture of TiH₂ and γ -Al₂O₃ nanopowder underwent initial mixing for 1 h in a powder mixer and was then inserted into the grooves, ensuring uniform filling. To prevent particle ejection during the process, the grooves were initially covered using a pinless 20-mm shoulder tool, with one covering pass for every two grooves. After

Fig. 1 Manufacturing process for localized (single groove) fabrication of precursor specimens

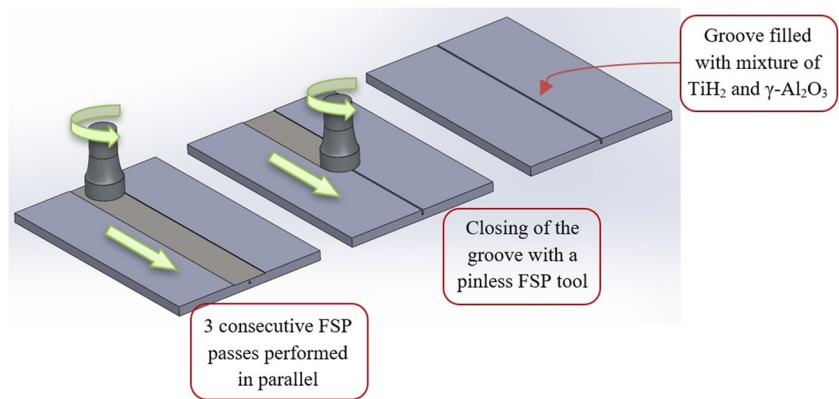
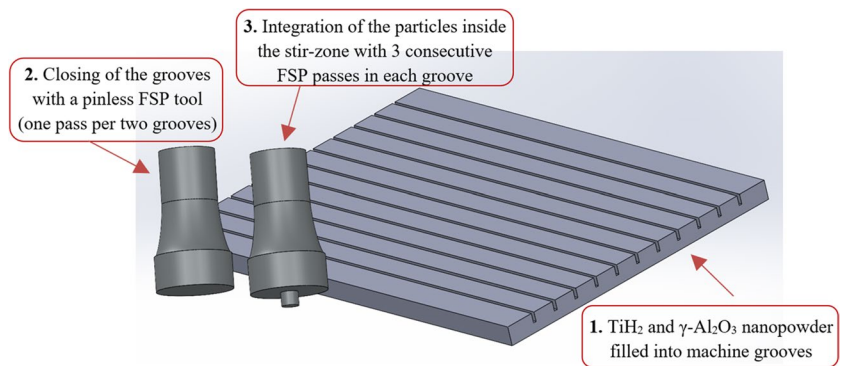


Fig. 2 Manufacturing process for large-scale (multiple grooves) fabrication of precursor specimens



the grooves were covered, three FSP passes were executed sequentially within each closed groove, maintaining the same direction, and ensuring that the samples did not cool down to room temperature between passes (the process is illustrated in Figs. 1 and 2). The higher number of FSP passes was chosen as it leads to a more uniform distribution of nanoparticles within the nugget for the AA5083. Subsequently, 1 mm was machined from the upper surface of the final precursor plate to eliminate introduced surface roughness and to avoid the “flow arm” area. The “flow arm” consists of thermomechanically affected material transferred from the retreating side of the stir zone to the advancing side material; thus, no reinforcing and foaming particles are integrated in the flow arm region.

The FSP experiments were conducted using a modified milling machine. The FSW tool was crafted from heat-treated steel, featuring a flat shoulder and a cylindrical threaded pin with a 22-mm shoulder diameter, a 5-mm pin diameter, and a 5-mm pin height. The choice of pin height was crucial as it determined the thickness of the layer enriched with reinforcing/stabilizing and foaming particles. In this particular instance, the pin height was intentionally selected to be 3 mm shorter than the thickness of the aluminum plate. This decision was made to create an aluminum skin on the surface of the foamed plate. The FSP parameters were configured based on prior research studies, with the

adopted operational parameters set at 1000 rpm rotational speed combined with a 13 mm/min transverse speed [22].

At the final manufacturing step, the precursor plate underwent thermal treatment in a preheated laboratory furnace to induce the foaming process, conducted at 700 °C with a holding time of 3 min. Following thermal treatment, the foamed plate was air-cooled to room temperature.

2.3 Compressive properties

In order to analyze the foam’s mechanical properties, specimens were machined from the initial foamed plate and submitted to uniaxial compression. Thus, electro discharge machining (EDM) was used to extract four samples out of the foamed plate and to create specimens of specific geometry (30 × 30 mm² cross-section and max height at 18 mm). Tests were performed in a universal testing machine (Instron 4482) at room temperature and ambient air and with a constant crosshead speed of 10 mm/min. The machine’s axis was parallel to the direction of the compression axis, and the samples were placed on the steady press base. A preload was applied to the samples until the gaps between the sample and jaws disappeared. The experiments automatically halted when the applied load exceeded the limit of 90 kN. This load ensured complete compressive deformation of the specimens, enabling the extraction of force/displacement data

beyond the densification point. Recorded force/displacement values were converted to stress/strain values based on the dimensions of the specimens. From the load–displacement acquired data, the stress–strain curves were created. From the stress–strain curves, the average compression strength, the Young’s modulus, the energy absorption, and the foams efficiency were obtained.

2.4 Macroscopical investigation of the porous structure

In both phases of this research, the porous structure was assessed through macroscopical investigation. The effective porosity was determined using graphical methods. Initially, EDM was employed to extract samples from the foamed batch, and stereoscopic images taken along the longitudinal axis of the FSP direction were utilized to calculate the average porosity of the foamed structures. The open-source image processing software, ImageJ, was employed to generate binary images of the pore structures (as shown in Fig. 4). Subsequently, porosity and the circularity of the pores were quantitatively evaluated.

3 Results and discussion

3.1 Study of the effect of blowing agent percentage

In Fig. 3, cross-sections of foamed specimens are presented with varying percentages of the blowing agent

TiH₂: (a) 0.3% w/w, (b) 0.5% w/w, (c) 0.7% w/w, and (d) 0.9% w/w. It is evident that even minor changes in the blowing agent percentage have a substantial impact on the foaming percentage and pore morphology.

An intriguing observation is that as the blowing agent percentage increases, the pores cannot remain confined within the foamed mixing zone (initial stir zone) and tend to move towards the region of the base material (a region without the presence of stabilizing particles). This is prominently visible in Fig. 3d, where, in the region outside the foamed mixing zone, some larger pores are formed. The size of these pores likely results from the absence of γ -Al₂O₃ nanoparticle stabilizers/reinforcers at the thermomechanical affected region outside the stir zone. This would pose a challenge in the creation of localized metal foams. However, in the context of producing large surface area reinforced metallic foam, it does not pose an issue since each mixing zone is in contact with neighboring mixing zones and not with the base material.

Table 1 presents the results of porous structure characterization. As expected, the foaming percentage increased with higher blowing agent percentages. The circularity of the pores did not exhibit significant variation. Consequently, for the large surface area reinforced metallic foam production stage, a blowing agent percentage of TiH₂ 0.9% w/w was selected.

Fig. 3 Foamed specimens with TiH₂ blowing agent percentages: **a** 0.3% w/w, **b** 0.5% w/w, **c** 0.7% w/w, **d** 0.9% w/w

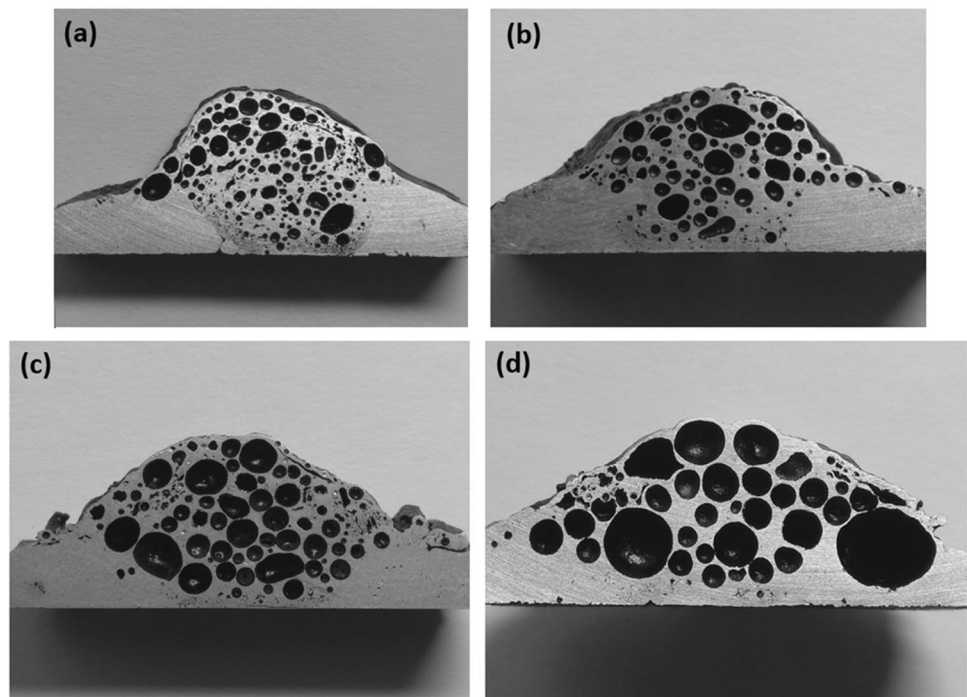


Table 1 Results of porous structure characterization

Foaming agent TiH ₂ (% w/w)	Max. porosity [95% CI=2%]	Circularity of pores [95% CI=0.04]
0.3	49%	0.85
0.5	60%	0.88
0.7	65%	0.89
0.9	68%	0.86

3.2 Uniaxial compression study

Initially, within the foamed plate, porosity (as shown in Fig. 4) was calculated using graphical methods. The foam exhibited a porosity level of 70%, with a pore circularity of 0.71. The decrease in circularity is logical, as the porosity has increased, and there is no adjacent matrix material for the pores to spread and develop spherically. The upper “skin” layer had an average thickness of 2.2 mm.

From the foamed plate, four specimens measuring 30×30

Fig. 4 Porous structure of the foamed plate

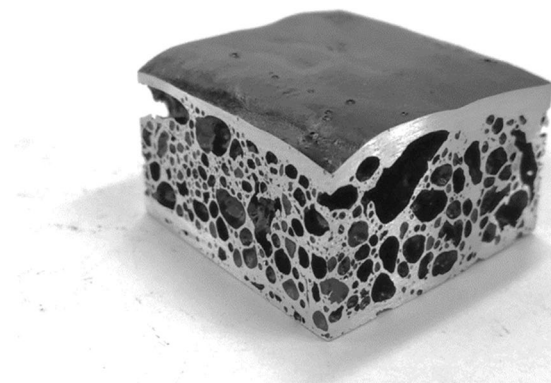
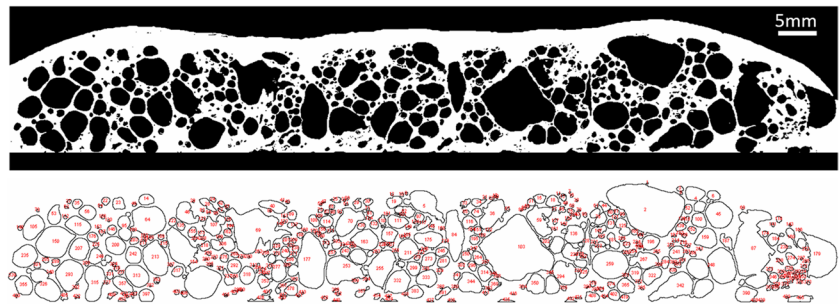


Fig. 5 Typical specimen of reinforced metal foam

mm² were cut, with an average height of 18 mm. Figure 5 displays a typical specimen of the reinforced metallic foam specimen. This specimen is characterized by a homogenous porous structure, while the skin surface exhibits slight curvatures, attributed to the geometric characteristics of the mixing zones.

Figure 6 presents the four specimens after uniaxial compression tests. In Fig. 7(a), the typical stress/strain curve is presented. Overall, the curve exhibits a smoothly evolving profile, devoid of significant fluctuations. This behavior suggests a non-brittle response of the foam, despite the presence of the ceramic reinforcement phase. More specifically, in the initial segment of the stress/strain curve, a relatively linear region is observed, extending up to the yield point. This

Fig. 6 Post-compression test specimens

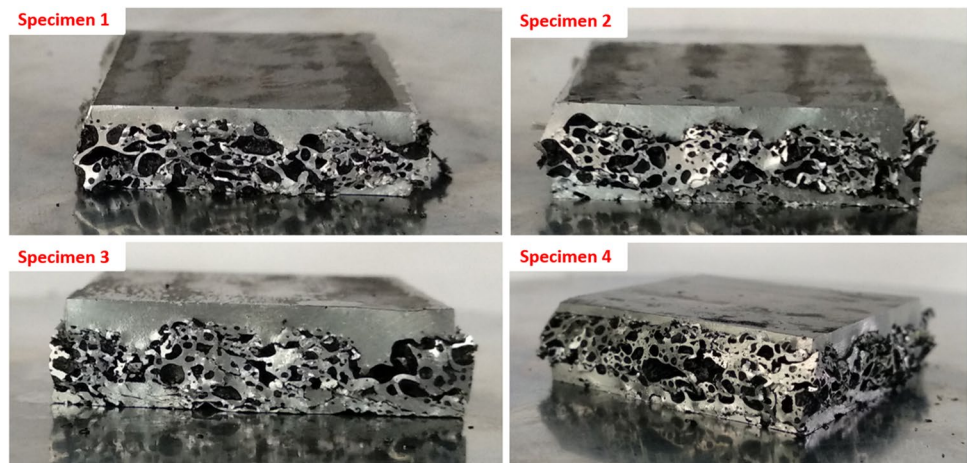
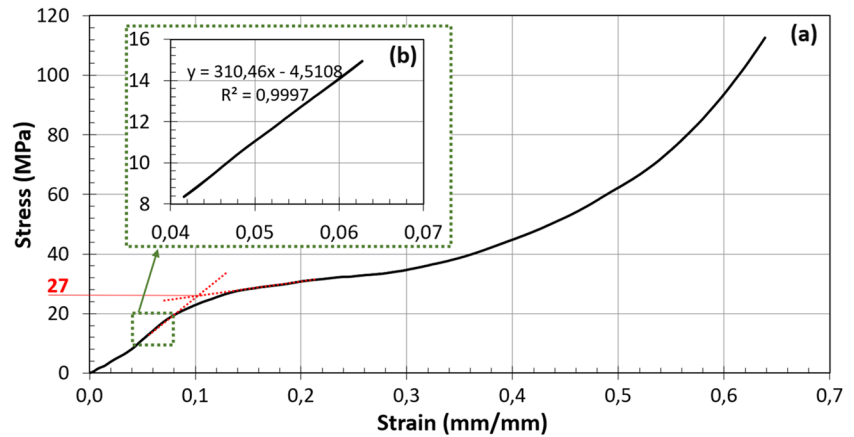


Fig. 7 **a** Stress–strain curve of reinforced aluminum foam, **(b)** region for Young’s modulus evaluation



region corresponds to the elastic zone of the specimen. As depicted in Fig. 7(a), the response in the elastic region can be distinguished into two consecutive regions with slightly different slopes. For strains from 0 to 0.04 (mm/mm), a smaller slope is observed, primarily attributed to the slight curvature of the upper specimen skin surface. In practice, this region terminates with the smoothing of the upper surface. The second region begins at a strain of 0.04 and stops at approximately 0.07 (mm/mm). From this segment, the elastic modulus was calculated, yielding a value of 0.310 GPa (Fig. 7(b)). This calculation was performed by using the least-squares method, with a coefficient of determination exhibiting a very high value of 0.9997. Correspondingly, the relative Young’s modulus was computed as 4.44×10^{-3} (ratio of Young’s modulus of the foam to the Young’s modulus of the bulk alloy [3]).

The critical stress, indicating the end of the elastic zone and the onset of foam collapse, is defined as the compressive strength. According to Ashby [3], this value is calculated differently depending on the shape of the stress/strain curve. In cases where a post-yield drop in stress is observed after the elastic region, it is defined as the peak just before the initiation of the drop. In cases where no stress drop is present after the elastic region (as in the stress/strain diagram in Fig. 7), the critical stress is graphically calculated from the intersection point of tangents

drawn to the segments of the σ - ϵ curve corresponding to the foam’s elastic zone and the plateau region. Thus, the critical stress was evaluated at 27 MPa.

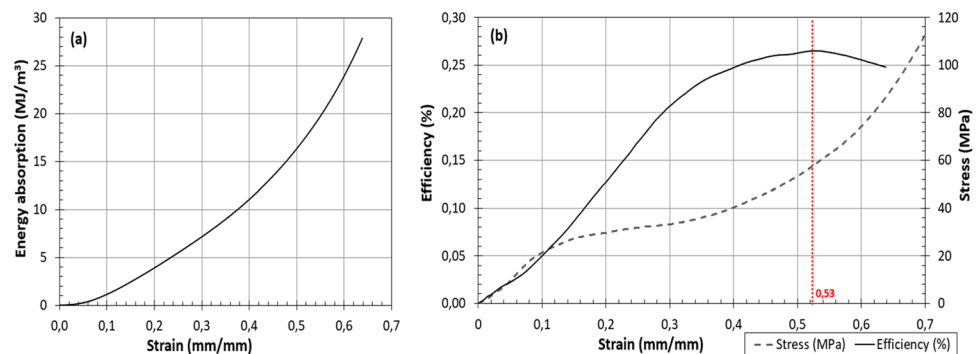
From the critical yield strength, we transition into the plateau region where the gradual collapse of the foam cells occurs. In the plateau region, there is plastic deformation of the cell walls, which manifests as bending and plastic buckling of the foam cell walls. Often, this mechanism is accompanied by the creation of macroscopic deformation zones. The stress in this region increases slightly. Moving from the plateau region, we enter the onset of densification region. In this region, there is complete collapse of the foam cells, resulting in a sudden increase in load. The onset strain of deformation is calculated from the foam’s energy yield diagram [3, 24]. Initially, the absorbed energy of the foam is calculated using the formula:

$$\text{Energy absorption}(e_a) = \int_0^{e_a} \sigma(e)de, 0 \leq (e_a) \leq 1$$

The corresponding foam energy absorption diagram, which is particularly useful as it provides values of absorbed energy for the entire range of deformations, is presented in Fig. 8a.

The energy absorbing efficiency (η) is calculated using the formula [3, 25, 26]:

Fig. 8 **a** Absorbed energy diagram, **b** energy absorption efficiency diagram



$$\eta(e_a) = \frac{\int_0^{e_a} \sigma(e)de}{\sigma_a}, 0 \leq (e_a) \leq 1$$

The densification strain, denoted as e_d , is defined as the point where the energy absorption efficiency reaches its maximum on the efficiency-strain curve, corresponding to the maximum value of e_i , where e_i represents the strain at that point[3, 25, 26]:

$$\left. \frac{d\eta(e_a)}{de} \right|_{e_a=e_i} = 0, 0 \leq (e_i) \leq 1$$

In the energy absorption efficiency diagram (Fig. 8b), the graphical calculation of the onset strain of densification is depicted in red, which corresponds to 0.53 mm/mm.

The stages of foam collapse are graphically illustrated in Fig. 9. From the test specimen images in the figure, it can be observed that in the plateau region, the initiation of cell collapse begins with deformation through bending of the struts at the larger pores. Subsequently, it gradually extends through macroscopic deformation zones and corresponding deformation mechanisms to the smaller cells.

Finally, Fig. 10a illustrates stress values for three characteristic strain levels, and in Fig. 10b, the corresponding energy absorption (per unit volume) is depicted for the same strain values. The charts also include error bars for the four specimens subjected to uniaxial compression. Stress and energy absorption values at 25% and 50% strain are particularly useful because they are employed in the comparison of foams produced.

3.3 Comparison of results

In Fig. 11, a correlation chart between the critical stress and porosity is presented for ALPORAS-type aluminum foams by Miyoshi et al. [27]. The critical stress obtained from the experiments in this study is denoted by a red asterisk (*). It is noteworthy that the critical stress is significantly higher compared to foams of similar porosity like ALPORAS foams.

Respectively, Fig. 12 presents the diagram illustrating the critical stress variation for different densities of aluminum (Al-12Si) foams produced using the IFAM manufacturing technology by Claar et al. [28]. For foams with similar

Fig. 9 Stages of Collapse in Reinforced Foams during Uniaxial Compression

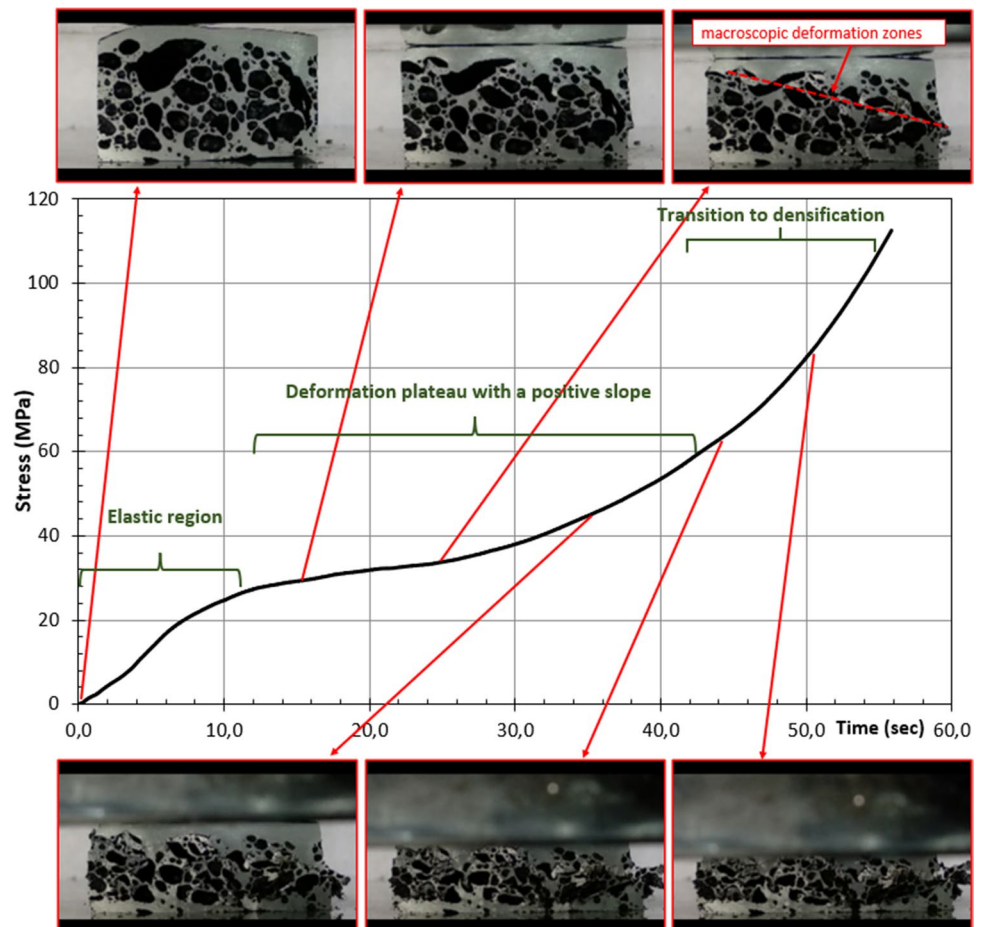


Fig. 10 Graphs of three characteristic strain values: **a** stress diagram, **b** energy absorption diagram

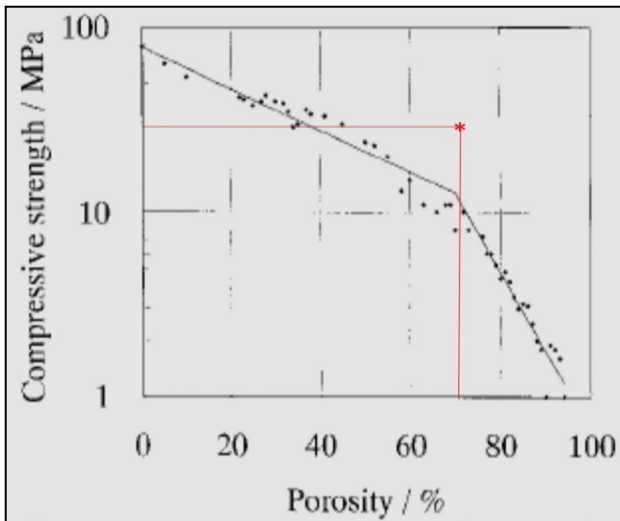
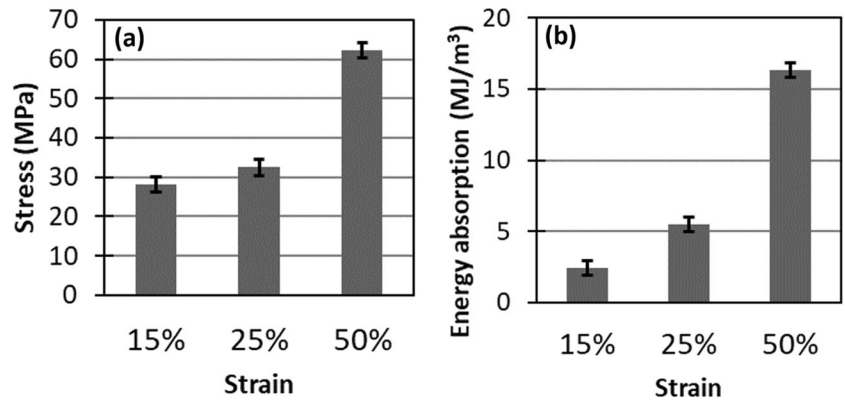


Fig. 11 Logarithmic diagram of the critical stress variation for different porosity values in ALPORAS-type foams by Miyoshi et al. [27] (the red asterisk (*) represents the critical stress value of the enhanced metallic foams from this research)

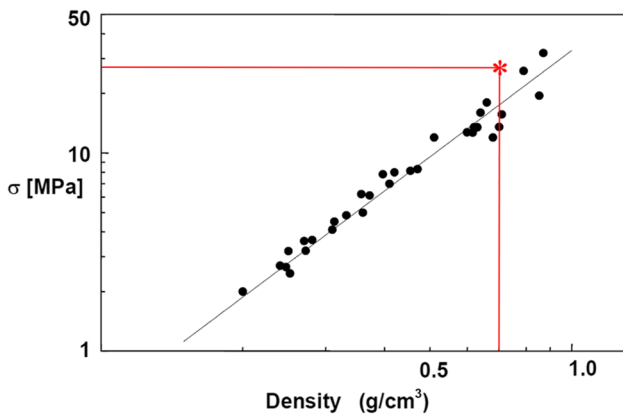


Fig. 12 Logarithmic diagram showing the variation of critical stress for different porosities in IFAM-type foams [28] (the value of critical stress for the enhanced metallic foams from the current research is marked with a red asterisk (*))

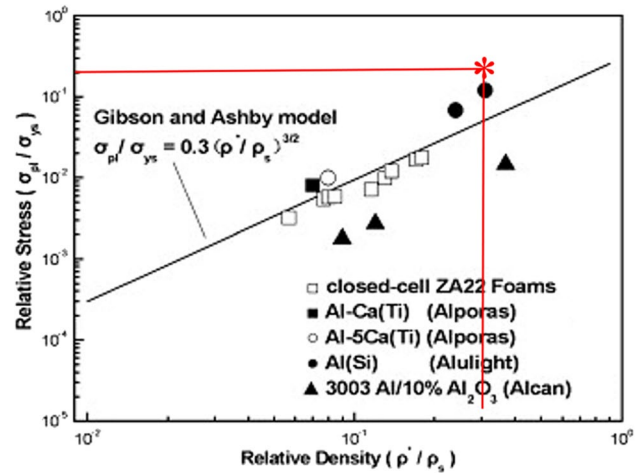


Fig. 13 Logarithmic plot of the variation of relative plateau stress for different porosities [30] (the red (*) denotes the value of the relative plateau stress for the enhanced metallic foams of the current study)

density in this research, the critical stress value is also shown to be increased.

In Fig. 13, the correlation diagram of relative plateau stress (relative critical stress) with relative density for various metallic foams from Liu et al. [29] is presented. The diagram correlates the values of relative plateau stress for different metallic foams with the theoretical values obtained from the equation proposed by Gibson and Ashby [3]:

$$\frac{\sigma_{pl}}{\sigma_{ys}} = c \left(\frac{\rho^*}{\rho_s} \right)^{3/2}$$

where c is a constant equal to 0.3 [29], σ_{pl} is the plateau stress, σ_{ys} is the yield strength of the base material, and ρ^* / ρ_s is the relative density of the foam. The red (*) denotes the relative plateau stress obtained from the experiments in the current study. The maximum value provided in the literature for AA5083-H111 was chosen as σ_{ys} . The relative plateau stress in this diagram is shown to have high values.

The comparison of the results with those found in the existing literature highlights the promising prospects for the foam structures reinforced through FSP. The notable improvements in mechanical properties observed in the composite metallic foams can be attributed to three key factors: (i) the inclusion of a reinforcing nano-crystalline phase of γ -Al₂O₃, (ii) the FSP approach, where we initiate from a bulk material for precursor development, and (iii) the deliberate selection of the non-heat-treatable AA5083 as the base material.

4 Conclusions

The successful development of reinforced aluminum foams in large dimensions using the single-plate approach and FSP process presents a significant leap forward in materials engineering and in particular for developing reinforced metallic foams. The critical stress, onset strain of densification, and relative Young's modulus were determined to be 27 MPa, 0.53 mm/mm, and 4.44×10^{-3} , respectively, showcasing substantial mechanical enhancement compared to conventionally produced foams. This approach eliminates the reliance on powder metallurgy techniques, addressing challenges associated with powder usage.

These advanced foams hold promise for revolutionizing industries through lightweight structural components, anti-ballistic materials, impact-resistant parts for the transport sector, and components requiring heightened stiffness and vibration absorption. The cost-effective and environmentally friendly production process aligns seamlessly with sustainable manufacturing practices, opening avenues for broader industrial adoption. In conclusion, the fabricated aluminum foam composites not only exhibit superior mechanical properties but also herald a new era of possibilities for industries seeking innovative, tailored, functionally graded materials.

Funding Open access funding provided by HEAL-Link Greece.

Declarations

Ethical approval Not applicable.

Conflict of interest The authors declare no competing interests.

Open Access This article is licensed under a Creative Commons Attribution 4.0 International License, which permits use, sharing, adaptation, distribution and reproduction in any medium or format, as long as you give appropriate credit to the original author(s) and the source, provide a link to the Creative Commons licence, and indicate if changes were made. The images or other third party material in this article are included in the article's Creative Commons licence, unless indicated otherwise in a credit line to the material. If material is not included in the article's Creative Commons licence and your intended use is not permitted by statutory regulation or exceeds the permitted use, you will

need to obtain permission directly from the copyright holder. To view a copy of this licence, visit <http://creativecommons.org/licenses/by/4.0/>.

References

1. Ashby MF, Lu T (2003) Metal foams: a survey. *Sci China, Ser B: Chem* 46(6):521–532. <https://doi.org/10.1360/02YB0203>
2. Banhart J (2001) Manufacture, characterisation and application of cellular metals and metal foams. *Prog Mater Sci* 46(6):559–632. [https://doi.org/10.1016/S0079-6425\(00\)00002-5](https://doi.org/10.1016/S0079-6425(00)00002-5)
3. Ashby MF, Evans A, Fleck NA, Gibson LJ, Hutchinson JW, Wadley HNG (2002) Metal foams: a design guide. *Mater Des* 23(1):119. [https://doi.org/10.1016/S0261-3069\(01\)00049-8](https://doi.org/10.1016/S0261-3069(01)00049-8)
4. Papantoniou I, Kyriakopoulou HP, Pantelis DI, Manolacos DE (2019) Metal foaming by powder metallurgy process: investigation of different parameters on the foaming efficiency. *Frattura ed Integrità Strutturale* 13(50):497–504. <https://doi.org/10.3221/IGF-ESIS.50.41>
5. Ma ZY (2008) Friction stir processing technology: a review. *Metall Mater Trans A Phys Metall Mater Sci* 39A(3):642–658. <https://doi.org/10.1007/S11661-007-9459-0/FIGURES/19>
6. Rodríguez A et al (2019) Burnishing of FSW aluminum Al–Cu–Li components. *Metals* 9(2):260. <https://doi.org/10.3390/MET9020260>
7. Sánchez Egea AJ, Rodríguez A, Celentano D, Calleja A, López de Lacalle LN (2019) Joining metrics enhancement when combining FSW and ball-burnishing in a 2050 aluminium alloy. *Surf Coat Technol* 367:327–335. <https://doi.org/10.1016/J.SURFCOAT.2019.04.010>
8. Papantoniou IG, Markopoulos AP, Manolacos DE (2020) A new approach in surface modification and surface hardening of aluminum alloys using friction stir process: Cu-reinforced AA5083. *Materials* 13(6):1278. <https://doi.org/10.3390/MA13061278>
9. Bagheri B, Abbasi M, Abdollahzadeh A, Mirsalehi SE (2020) Effect of second-phase particle size and presence of vibration on AZ91/SiC surface composite layer produced by FSP. *Trans Nonferrous Metals Soc China* 30(4):905–916. [https://doi.org/10.1016/S1003-6326\(20\)65264-5](https://doi.org/10.1016/S1003-6326(20)65264-5)
10. Abdollahzadeh A, Bagheri B, Abbasi M, Sharifi F, Ostovari-Moghaddam A (2021) Mechanical, wear and corrosion behaviors of AZ91/SiC composite layer fabricated by friction stir vibration processing. *Surf Topogr* 9(3):035038. <https://doi.org/10.1088/2051-672X/AC2176>
11. Abbasi M, Givi M, Bagheri B (2019) Application of vibration to enhance efficiency of friction stir processing. *Trans Nonferrous Metals Soc China* 29(7):1393–1400. [https://doi.org/10.1016/S1003-6326\(19\)65046-6](https://doi.org/10.1016/S1003-6326(19)65046-6)
12. Vakili-Azghandi M, Roknian M, Szpunar JA, Mousavizade SM (2020) Surface modification of pure titanium via friction stir processing: microstructure evolution and dry sliding wear performance. *J Alloys Compd* 816:152557. <https://doi.org/10.1016/J.JALLCOM.2019.152557>
13. Węglowski MS (2018) Friction stir processing – state of the art. *Arch Civil Mech Eng* 18(1):114–129. <https://doi.org/10.1016/J.ACME.2017.06.002>
14. Bagheri B, Abdollahzadeh A, Abbasi M, Kokabi AH (2021) Effect of vibration on machining and mechanical properties of AZ91 alloy during FSP: modeling and experiments. *Int J Mater Form* 14(4):623–640. <https://doi.org/10.1007/S12289-020-01551-2/FIGURES/16>
15. Olhan S, Khatkar V, Behera BK (2023) Novel high-performance textile fibre-reinforced aluminum matrix structural composites fabricated by FSP. *Mater Sci Eng, B* 289:116265. <https://doi.org/10.1016/J.MSEB.2023.116265>

16. Darji R, Joshi G, Badheka V, Patel D (2023) Applications of friction-based processes in manufacturing. *Lecture Notes in Mechanical Engineering*, pp. 236–243. doi: https://doi.org/10.1007/978-981-16-9523-0_27/FIGURES/3.
17. Hangai Y, Utsunomiya T (2009) Fabrication of porous aluminum by friction stir processing. *Metall Mater Trans A Phys Metall Mater Sci* 40(2):275–277. <https://doi.org/10.1007/S11661-008-9733-9/FIGURES/3>
18. Hangai Y, Utsunomiya T, Hasegawa M (2010) Effect of tool rotating rate on foaming properties of porous aluminum fabricated by using friction stir processing. *J Mater Process Technol* 210(2):288–292. <https://doi.org/10.1016/J.JMATPROTEC.2009.09.012>
19. Utsunomiya T, Tamura KI, Hangai Y, Kuwazuru O, Yoshikawa N (2010) Effects of tool rotating rate and pass number on pore structure of A6061 porous aluminum fabricated by using friction stir processing. *Mater Trans* 51(3):542–547. <https://doi.org/10.2320/MATERTRANS.MBW200916>
20. Hangai Y, Saito K, Utsunomiya T, Kuwazuru O, Yoshikawa N (2014) Fabrication and compression properties of functionally graded foam with uniform pore structures consisting of dissimilar A1050 and A6061 aluminum alloys. *Mater Sci Eng, A* 613:163–170. <https://doi.org/10.1016/J.MSEA.2014.06.039>
21. Papantoniou IG, Kyriakopoulou HP, Pantelis DI, Manolacos DE (2018) Fabrication of MWCNT-reinforced Al composite local foams using friction stir processing route. *Int J Adv Manuf Technol* 97(1–4):675–686. <https://doi.org/10.1007/S00170-018-1964-3/METRICS>
22. Papantoniou IG, Kyriakopoulou HP, Pantelis DI, Athanasiou-Ioannou A, Manolacos DE (2018) Manufacturing process of AA5083/nano- γ -Al₂O₃ localized composite metal foam fabricated by friction stir processing route (FSP) and microstructural characterization. *J Mater Sci* 53(5):3817–3835. <https://doi.org/10.1007/S10853-017-1802-2/FIGURES/21>
23. Hashim J, Looney L, Hashmi MSJ (2001) The wettability of SiC particles by molten aluminium alloy. *J Mater Process Technol* 119(1–3):324–328. [https://doi.org/10.1016/S0924-0136\(01\)00975-X](https://doi.org/10.1016/S0924-0136(01)00975-X)
24. Michailidis N, Stergioudi F, Tsouknidas A (2011) Deformation and energy absorption properties of powder-metallurgy produced Al foams. *Mater Sci Eng, A* 528(24):7222–7227. <https://doi.org/10.1016/J.MSEA.2011.05.031>
25. Li QM, Magkiriadis I, Harrigan JJ (2006) Compressive strain at the onset of densification of cellular solids. *42(5)*: 371–392. <https://doi.org/10.1177/0021955X06063519>
26. Shen J, Lu G, Ruan D (2010) Compressive behaviour of closed-cell aluminium foams at high strain rates. *Compos B Eng* 41(8):678–685. <https://doi.org/10.1016/J.COMPOSITESB.2010.07.005>
27. Miyoshi T, Itoh M, Akiyama S, Kitahara A. ALPORAS aluminum foam: production process, properties, and applications. doi: [https://doi.org/10.1002/\(SICI\)1527-2648\(200004\)2:4](https://doi.org/10.1002/(SICI)1527-2648(200004)2:4)
28. Claar TD, Yu CJ, Hall I, Banhart J, Baumeister J, Seeliger W (2000) Ultra-lightweight aluminum foam materials for automotive applications. *SAE Techn Papers*. <https://doi.org/10.4271/2000-01-0335>
29. Liu J, Yu S, Zhu X, Wei M, Luo Y, Liu Y (2008) The compressive properties of closed-cell Zn-22Al foams. *Mater Lett* 62(4–5):683–685. <https://doi.org/10.1016/J.MATLET.2007.06.032>
30. Liu J, Yu S, Zhu X, Wei M, Luo Y, Liu Y (2009) Correlation between ceramic additions and compressive properties of Zn-22Al matrix composite foams. *J Alloys Compd* 476(1–2):220–225. <https://doi.org/10.1016/J.JALLCOM.2008.09.069>

Publisher's Note Springer Nature remains neutral with regard to jurisdictional claims in published maps and institutional affiliations.